Nano Research
2022, 15(3): 2689–2696

ISSN 1998-0124 CN 11-5974/O4
https://doi.org/10.1007/s12274-021-3790-4

Research Article

Binary-ternary transition metal chalcogenides interlayer coupling in van der Waals type-II heterostructure for visible-infrared photodetector with efficient suppression dark currents

Guoliang Xu[1], Danmin Liu[1] (✉), Songyu Li[2], Yi Wu[1], Zhenlu Zhang[3], Shaobo Wang[1], Zikun Huang[1], and Yongzhe Zhang[4] (✉)

[1] *Key Laboratory of Advanced Functional Materials, Ministry of Education, Faculty of Materials and Manufacturing, Beijing University of Technology, Beijing 100124, China*
[2] *School of Physics and Nuclear Energy Engineering, Beihang University, Beijing 100083, China*
[3] *School of Science, Beijing University of Posts and Telecommunications, Beijing 100876, China*
[4] *Key Laboratory of Optoelectronics Technology, Ministry of Education, Faculty of Information Technology, Beijing University of Technology, Beijing 100124, China*

Received: 4 May 2021 / **Revised:** 14 July 2021 / **Accepted:** 3 August 2021

ABSTRACT

Ternary two-dimentional (2D) materials exhibit diverse physical properties depending on their composition, structure, and thickness. Through forming heterostructures with other binary materials that show similar structure, there can be numerous potential applications of these ternary 2D materials. In this work, we reported the structure of few-layer $CrPS_4$ by X-ray diffraction, transmission electron microscope, and electron-density distribution calculation. We also demonstrated a new application of the $CrPS_4/MoS_2$ heterobilayer: visible-infrared photodetectors with type-II staggered band alignment at room temperature. The response of the heterostructure to infrared light results from a strong interlayer coupling that reduces the energy interval in the junction area. Since the intrinsic bandgap of individual components determines wavelengths, the decrease in energy interval allows better detection of light that has a longer wavelength. We used photoluminescence (PL) spectroscopy, Kelvin probe force microscopy (KPFM) under illumination, and electrical transport measurements to verify the photoinduced charge separation between the $CrPS_4/MoS_2$ heterostructures. At forward bias, the device functioned as a highly sensitive photodetector, as the wavelength-dependent photocurrent measurement achieved the observation of optical excitation from 532 to 1,450 nm wavelength. Moreover, the photocurrent caused by interlayer exciton reached around 1.2 nA at 1,095 nm wavelength. Our demonstration of the strong interlayer coupling in the $CrPS_4/MoS_2$ heterostructure may further the understanding of the essential physics behind binary-ternary transition metal chalcogenides heterostructure and pave a way for their potential applications in visible-infrared devices.

KEYWORDS

heterostructure, MoS_2, $CrPS_4$, interlayer transition, visible-infrared photodetector, type-II band alignment

1 Introduction

Since the discovery of atomically thin graphene by Novoselov et al., research interests in layered materials, particularly in heterostructures of two-dimentional (2D) materials, have burgeoned in the microelectronic field [1]. Comparing to individual 2D materials, heterostructures possess additional functions and allow more freedom in the structure design, and these advantages have made heterostructures as one of the dominating research. To create different heterostructures and examine their functions, studies have adapted mechanical exfoliation, for its versatility, as a protocol to fabricate heterostructures of monolayers from different van der Waals (vdW) crystals. Among the various forms of heterostructures, binary transition metal dichalcogenide (TMD)-based heterostructures have been found to have multiple novel functions, such as the artificial superlattice yielding Hofstadter's butterfly [2], bandgap engineered devices [3], efficient light-emitting diodes [4], and photodetectors [5]. Through vertically artificial stacking two different TMDs, type-II band alignment can be acquired, forming a new type of optically active heterojunction. For instance, type-II heterostructure MX_2/MX_2 (M = Mo, W; X = S, Se, Te) has been reported to show unique photoelectric responses with an interband transition ranging from infrared to visible wavelengths [6, 7]. The type-II staggered band alignment creates the condition for heterostructures to generate interlayer optical excitation, modulate the interlayer transition energy, and induce the charge spatial separation [8, 9], due to the fact that the conduction band minimum and valence band maximum belong to two independent components as well as electrons and holes confined to opposite layers.

Given that the particular structures of TMDs heterostructures enable their interlayer transition excitation, one may wonder

Address correspondence to Danmin Liu, dmliu@bjut.edu.cn; Yongzhe Zhang, yzzhang@bjut.edu.cn

whether transition metal thiophosphates (TMTs), which have similar structures as TMDs, are possible for strong interlayer coupling with TMDs as well. TMTs, a group of ternary transition metal chalcogenides with the formula MPS_3 or MPS_4 (where M denotes metal, P denotes phosphorous, and S denotes sulfur), have rarely been studied despite of their rich magnetic properties and their distinctive semiconducting characteristics [10, 11]. Among various types of TMTs, chromium thiophosphate ($CrPS_4$), given its unique semiconducting characteristics [12, 13] revealed by PL measurements with optical band gap between 1.3 and 1.5 eV, is considered as a promising infrared material that should deserve more examination. Therefore, we hypothesized that because of the similarity in atomic structures of TMTs and TMDs, binary-ternary transition metal chalcogenides heterostructures, specifically $CrPS_4$-based heterostructures, may show strong interlayer coupling. The reason why we fabricated such a heterostructure includes two reasons. The first reason is that the work function of $CrPS_4$ is 3.84 eV, while MoS_2 is 4.37 eV. A type-II heterostructure forms with the two suitable work functions. The second is that the nearest latices distance at $(1\bar{1}0)$ direction for MoS_2 is 5.488 Å, while the nearest latices distance at (100) direction for $CrPS_4$ (CPS) is 5.435 Å. When we stack angle-shaped CPS on top of MoS_2, periodic latices mismatch forms as shown in Fig. S8 in the Electronic Supplementary Material (ESM). Different latices mismatch and stacking arrangements can cause the change of periodic potential. Periodic potential affects the electronic band structure and the electron wavefunction in the heterostructure within the mini-Brillouin zone [6]. The electronic band structure dominates over strength of interlayer excitons. Thus we use angle-shaped CPS to fabricate heterostructure with MoS_2. And such heterostructures can induce added performances, including interlayer transition excitation, which is crucial for developing potential applications that relate to optical communication, environmental monitoring, medical diagnostics, and even missile early warning [8, 14–17].

In this work, we report a comprehensive study on exfoliated CPS and few-layer CPS/MoS_2 heterostructure. First, high-quality bulk CPS crystals were synthesized from elements using chemical vapor transport (CVT) method. The composition and microstructure of the bulk $CrPS_4$ crystals were determined by the following methods: X-ray diffraction (XRD), high-resolution transmission electron microscope (HR-TEM) with energy dispersive spectroscopy (EDS), optical investigation Raman spectroscopy, and photoluminescence (PL). To verify the possible light detection ability in CPS/MoS_2 heterostructure, we used angle-shaped CPS to fabricate CPS/MoS_2 heterostructure (Fig. 6(a)) via mechanical exfoliation and target-transfer techniques. The thicknesses of CPS and MoS_2 were confirmed by atomic force microscope (AFM) as ~ 7 and 6 nm, corresponding to eleven layers (11L) and eight layers (8L), respectively. Then, we realized visible-infrared photodetection (532–1,450 nm) based on a type-II CPS/MoS_2 heterostructure in which individual CPS and MoS_2 show no response beyond the limits of the intrinsic band gap but the interlayer coupling in CPS/MoS_2 heterostructure shrinks the energy intervals of electrons transition to make an infrared photodetector possible. The interlayer coupling interaction between CPS and MoS_2 results in a type-II staggered band alignment, which can be confirmed using a PL change, Kelvin probe force microscopy (KPFM), and electrical transport measurements. We also calculated the electron-density distribution (EDD) by the maximum entropy method (MEM) from the structure factor data deduced from directly experimental XRD data to determine the types of chemical bonds in CPS. As a result, the CPS/MoS_2 heterostructure can be operated at extremely low dark currents (10^{-10} A) and possesses a high distinct photocurrent response in the infrared region. Therefore, the creation of type-II CPS/MoS_2 heterostructure paves a new way to manipulate optoelectronics devices exploiting interlayer excitons and design next-generation infrared optoelectronics.

2 Results and discussion

2.1 Exfoliated $CrPS_4$ with structural characterization

CVT method is used to synthesize CPS crystal. The XRD measurement is facilitated to analysis crystal orientation nature of vdW bulk crystal, though a flake is positioned parallel to the substrate. It can be seen that the CPS crystal precisely acquires the diffraction peak as shown by the black curve in Fig. 1(a), coincident with the (001), (002), (003), (004), and (005) peaks, indicating that CPS stacks layer by layer along the *c*-axis. The inset in Fig. 1(a) shows single crystal diffraction pattern with bright dots on concentric. This indicates high quality single CPS is synthesized. The CPS crystal has a monoclinic structure which has been reported by Diehl and Carpentier [18]. It belongs to the space group C121 and its lattice constants are a = 10.871Å, b = 7.254Å, c = 6.140Å, $\alpha = \gamma = 90°$, and β = 91.88°, respectively. The deliberate structure is shown in Figs. 1(b)–1(d) with three view orthographic projections and lattice unit cell is mark by a rectangle. Inside a single layer with five atoms thick, each Cr and P atom are bonded with six and four adjacent S atoms to form a CrS_6 octahedron and PS_4 tetrahedron unit respectively (Fig. S1 in the ESM) [19]. In view of the *ac* plane, CPS belongs to the category of layered materials since it has weak van der Waals gaps between sulfur layers. Thus, micron thin flakes could be easily isolated using the well-known Scotch tape method. A representative photo image of a produced single crystal is shown

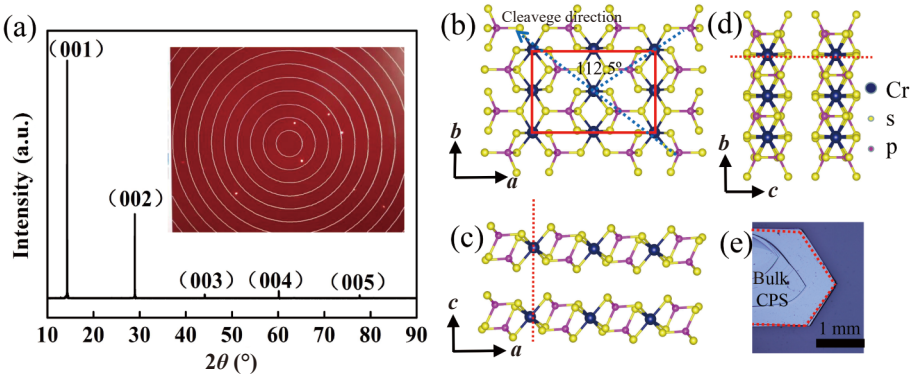

Figure 1 Crystal lattice structure and bulk sample of CPS (a) X-ray diffraction pattern of CPS crystal. Inset of Fig. 1(a) shows single crystal XRD. (b)–(d) Third angle orthographic projection of CPS atomic structure model. Gray-blue, yellow, and purple spheres represent Cr, S, and P atoms, respectively. The red line shows the lattice unit cell. (e) Bulk crystal sample of CPS.

in Fig. 1(e) with preferred crystallographic directions as marked in the image by red line. It is found crystal growth orientation is the same as the direction of cleavage of thin crystals as shown in Fig. 2(a).

A TEM image of a selected CPS flake is presented in Fig. 2(a), showing straight edges with formed characteristic angles (112.5 deg). By comparing the lattice structure model with high resolution STEM, we find that the preferred edges are aligned along the Cr diagonal atomic alignment directions lying in the (110) and ($1\bar{1}0$) plane (red line in Fig. 2(b)). Thus, it is worth noting that CPS crystals tend to be easily torn along the diagonal direction of Cr atoms [19]. This analysis provides an easy tool to determine the crystallographic orientation of exfoliated CPS and can be readily used in studying orientation-dependent physical properties. Thus, the twist angle of CPS-based bilayer can be readily determined through the relative orientation of the top and bottom triangle shapes. A diffraction pattern acquired in the selected flake is shown in the inset of Fig. 2(a), which has a clear monoclinic structure confirming the nature of high single crystalline corresponding well with the XRD results in Fig. 1(b). The HR-TEM image of the sample in Fig. 2(b), acquired by liquid exfoliated, shows clear lattice fringes and atomic arrangement. The heavy metal element Cr shows white spots (red point) while the light non-metallic element S (yellow point) and P (purple point) show gray-black spots. We can identify the lattices of Cr atoms are 5.25 and 3.47Å, which are very close to the literature's results [20]. The composition of a CPS flake confirmed by energy-dispersive X-ray spectroscopy spectrum shown in Fig. S2 in the ESM shows strong signals of Cr, P, and S with mole ratios 1:1:4, which matches well with the stoichiometry of CPS. The corresponding elemental mapping clearly reveals the uniform element distribution and layered structure in the CPS flake as shown in Fig. S2 in the ESM.

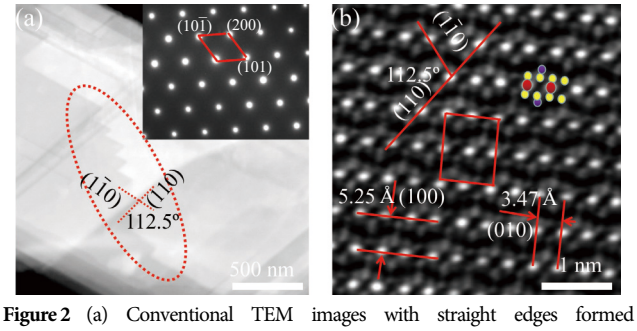

Figure 2 (a) Conventional TEM images with straight edges formed preferential angles as marked in the image. The inset shows its diffraction pattern and single crystallinity. (b) High-angle annular dark-field scanning transmission electron microscopy (HAADF-STEM) image in high magnification clearly reveals atom alignment of a few-layered sample.

2.2 Strong interlayer coupling and interlayer excitation process

To theoretically examine the profile of surface electronic in CPS crystals, an accurate method is used to calculate the EDD from the structure factor data deduced directly from X-ray diffraction data by the MEM, which is different from traditional density-function theory (DFT) calculations in theory. Thus, the accessible data of EDD are actual because of any approximations and human factors non-existent [21]. The experimental 3D EDD by the MEM is shown in Figs. 3(a)–3(c). It is clearly found that EDD results in Fig. 3(a) are almost the same with crystal structure shown in Figs. 1(a) and 2(b) except for the extra electron distribution between layers, as shown in red dotted rectangle in Fig. 3(b). This is because one P atom has five valence electrons, but only four are connected by covalent bonds forming PS_4 tetrahedron unit as shown in Fig. S1 in the ESM. Therefore, we have reasons to suppose that interlayer interaction, in some ways, may benefit from the unbonded electron during fabrication with another 2D materials. On this basis, it is natural that a CPS with MoS_2 heterostructure has been fabricated to analysis its interlayer coupling as shown in Fig. 3(d) with the schematic illustration of the device layout. To probe the interlayer excitation process, a more specific calculation (Fig. 3(e)) is done to predict the interval energy interval in the CPS/MoS_2 heterostructure. We know that there is an intrinsic response cutoff wavelength of 678 nm (1.83 eV) for MoS_2 and 843 nm (1.47 eV) for CPS. The possible interlayer transitions in the heterojunction are illustrated by arrows with a gap about 0.84 eV (~ 1,476 nm) from the valence band maximum of CPS to the conduction band minimum of MoS_2 locating in near infrared spectral range. Therefore, such a type-II heterostructure device can allow a transition from valence band of CPS to conduction band of MoS_2 under infrared light with the wavelength longer than 843 nm.

2.3 Raman and photoluminescence spectroscopy of heterostructure

Raman spectroscopy is sensitive to phonon behaviors or the interlayer interaction in layered 2D atomic crystals and is shown in Fig. 4(a) from the individual materials as well as the overlap region (measured with laser wavelength of 532 nm at junction area). CPS has a much more complex Raman spectrum, herein we

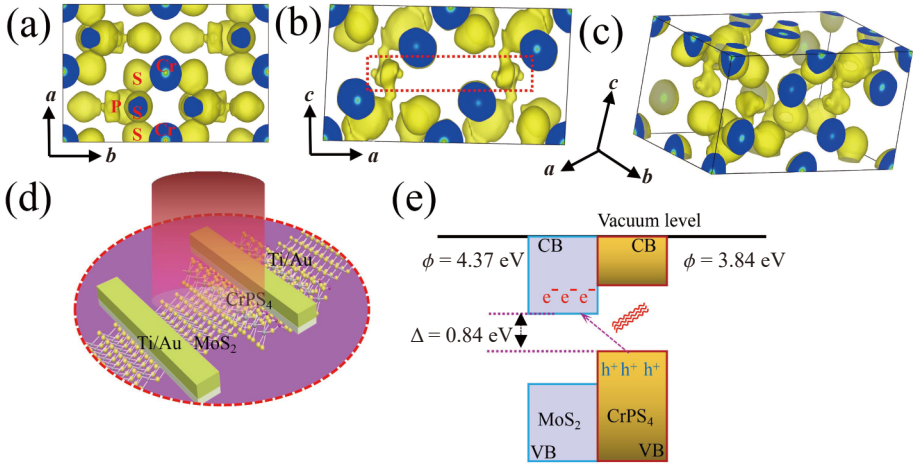

Figure 3 MEM electron-density distributions of CPS and band gap alignment of CPS/MoS_2 heterostructure. (a)–(c) The electron density of CPS calculated by MEM. (d) Schematic diagram of a CPS/MoS_2 vdW heterostructure device under infrared light excitation. (e) Corresponding schematic illustrations of type-II interlayer energy interval in CPS/MoS_2 vdW heterostructure.

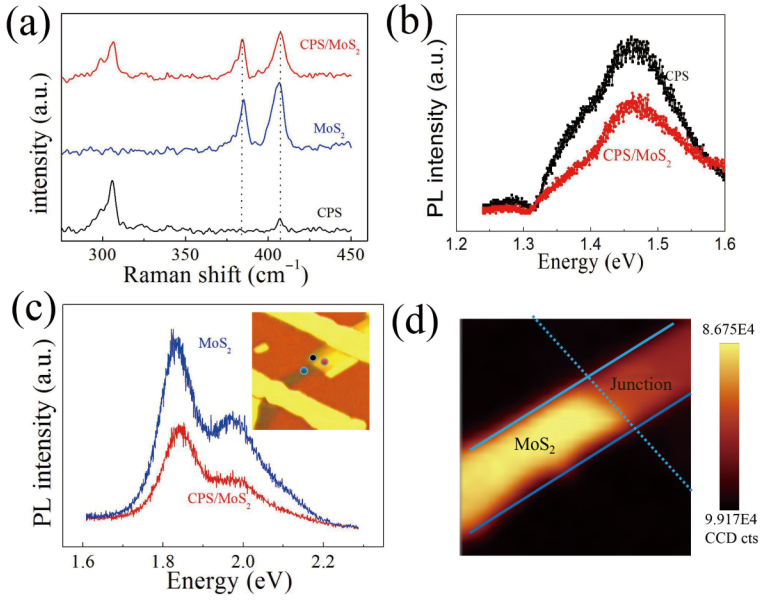

Figure 4 Crystalline vibration and PL analysis of the CPS/MoS_2 vdW heterostructure. (a) Raman spectrum of the heterostructure. The tested position is marked by a red, blue, and black dot inset of part c. (b) and (c) Comparison of PL spectra between individual components and heterojunction area. (d) PL mapping of the emission at about 1.83 eV (MoS_2).

just introduce the obvious main peaks located at ~ 298, 306, and 407 cm^{-1}. The detailed Raman spectrum of CPS is presented in Fig. S3 in the ESM. MoS_2 shows two distinct Raman peaks at ~ 383 and 407 cm^{-1}, corresponding to in-plane E_{2g} and out of plane A_{1g} vibrations [22]. Specifically, the overlap region with insensitive Raman shifting exhibits almost the same Raman peak positions of the combination of CPS and MoS_2 (298, 306, 385, and 407 cm^{-1}), which actually is in accord with reported works [23]. Meanwhile, it can be clearly noticed that Raman peaks both appear in individual CPS and MoS_2 at 407 cm^{-1}, assigned to out-of-plane A_{1g} phonon modes. Previous Raman studies suggest that the similar vibrational modes are directly related to the interlayer coupling [23], which has the potential to probe the interface coupling in folded (or twisted) heterostructure built from TMDs. Thus, we can infer that vdW heterostructure interface between CPS and MoS_2 has strong electron–phonon interactions through similar lattice vibration. This electron–phonon interactions affect phonon relaxation (i.e., decay of the optical phonons into the acoustic phonons) at vdW heterostructure interface, which has a direct influence on carrier relaxation rate (Electron mobility is limited by acoustic phonon scattering) [24].

The charge transfer process at CPS/MoS_2 interface can also induce remarkable quenching effect [25] of PL intensity, as seen in Figs. 4(b) and 4(c), which further verifies the interlayer coupling effects in heterostructure. It is apparent that CPS and MoS_2 individual materials show strong PL at their respective exciton resonances (1.47 and 1.83 eV), and found both PL signals are efficiently quenched in CPS/MoS_2 heterostructure. Accordingly, the observation of reduced PL from both CPS and MoS_2 exciton resonances at heterostructure area demonstrates that efficient charge separation takes place in this type II heterostructure. To further unveil the quenching effect, PL mapping study is performed to study on the whole heterostructure as shown in Fig. 4(d). It is observed that the PL intensity of MoS_2 at heterojunction area shows obvious attenuation line of demarcation compared with pristine part. Such a quenching phenomenon strongly evidences the charge separation at junction area. Herein we also observe two PL peaks in CPS located at 1.47 and 1.28 eV. The two emission peaks are attributed to the lowest spin-allowed d–d optical transitions of Cr^{3+} ions, ($^4A_{2g} \rightarrow {}^4T_{2g}$ and $^4A_{2g} \rightarrow {}^4T_{1g}$), as have been observed in many other Cr-based compounds [26].

2.4 Type II heterostructure confirmed by KPFM

To further conform type II staggered band alignment and charge transfer in CPS/MoS_2 heterostructure, an *in situ* AFM topography and KPFM surface potential are utilized to unveil the charge transfer of heterostructure in the dark and light conditions [27], as shown in Figs. 5(a)–5(c). KPFM quantitatively measures the surface potential difference (SPD) between sample surface and tip; therefore, the relative potential gradient change representing charge transfer in heterostructure can be directly identified. Figure 5(b) shows an apparent SPD about 105 mV (Fig. S4 in the ESM) between CPS and junction produced under dark. This is because the work function of MoS_2 (Φ_{MoS_2}) is larger than that of CPS (Φ_{CPS}). Figures 5(b) and 5(c) demonstrate the SPD pictures of the junction area in dark and under illumination for comparison (region I indicated in Fig. 5(a)). Although the SPD change in the static figure is obvious, one can more easily judge from dynamic Fig. S5 in the ESM that CPS changes to higher potential and junction to smaller. This strongly evidences that the photo-generated electron–hole pairs have been separated to CPS (holes) and MoS_2 (electrons) [8, 28], respectively. The energy band diagrams of CPS/MoS_2 heterostructure in dark and light conditions are shown in Figs. 5(d) and 5(e). The heterostructure forms a type-II band alignment and CPS/MoS_2 Fermi levels align in equilibrium condition (in the dark). Upon illumination, many photoinduced holes and electrons are generated. Subsequently, the type-II band alignment of the CPS/MoS_2 heterostructure will lead to electrons flow from low potential to high potential, causing separated holes and electrons residing in two different materials. Furthermore, in two-dimensional heterostructures with type II band alignment, the spatially separated electron and hole with large binding energy remain strong Coulomb interaction and thus form a tightly bound interlayer exciton, where Coulomb bound electrons and holes are confined to opposite layers. Thus, the interface becomes a carrier accumulation layer but not a carrier depletion layer [31]. As a result, there are more electrons injected from CPS into MoS_2 which further lowers the work function of MoS_2 and the quasi-Fermi levels of these two materials shift in opposite directions thus a different SPD can be measured.

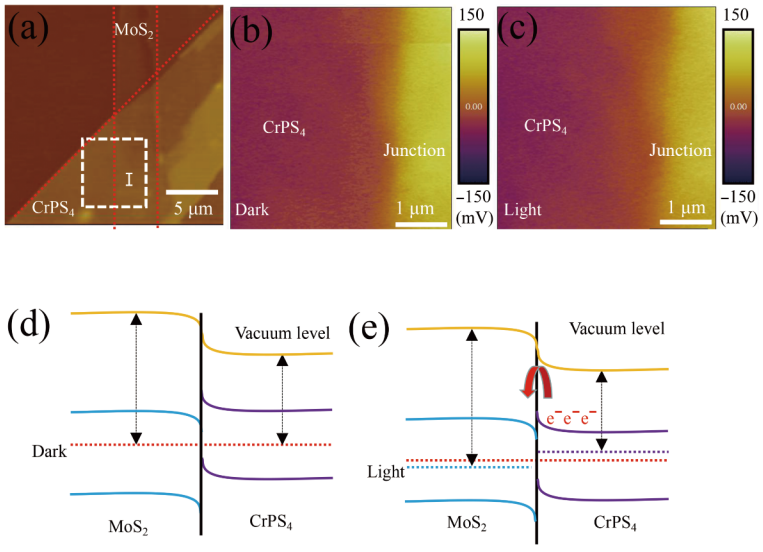

Figure 5 KPFM measurement of CPS/MoS_2 vdW heterostructure with 532 nm laser. (a) The *in situ* AFM measurements for surface morphology. (b) and (c) Surface potential images in the region I under dark and light. (d) and (e) The energy band alignment for CPS/MoS_2 vdW heterostructure in dark and light, respectively.

2.5 Visible-infrared photodetection of CPS/MoS_2 device

To better understand the photoresponse mechanism for this type-II band alignment in the interlayer coupling heterostructure, we have fabricated photodetector based on this CPS/MoS_2 heterostructure on silicon wafer (285 nm SiO_2) as shown in Fig. 6(a). Figure 6(b) shows the schematic illustration of the device layout. We use angle-shaped [33] CPS bilayers to stack with MoS_2 by mechanical exfoliation which angle is 67.5° consistent with the Cr diagonal atomic alignment directions in Fig. 2(b). Therefore, we can determine the twist angle of CPS/MoS_2 heterostructure from the relative rotation of the two vertically stacked materials. The schematic band diagrams are shown in Fig. 6(c). When the junction is under 0 bias, the charges generated by illumination are separated at the overlapped region confirmed by KPFM in Fig. 5. Under photoexcitation beyond intrinsic transition, electron–hole bound pairs (excitons) are generated in MoS_2 and CPS monolayers. As excitons have less energy than the unbound electrons and holes, their energy levels lie in between the valence band (VB) and conduction band (CB) in both the layers by considering exciton binding energy. Then, the electrons in VB of CPS transfer CB of MoS_2 to form interlayer excitons. This results in the majority carriers in MoS_2 are electrons while the majority carriers in CPS are holes. Finally, owing to the type-II band alignment of the heterostructure, the photoexcited electrons and holes relax to the CB edge of MoS_2 and the VB edge of CPS, respectively, via the interlayer relaxation process. Under forward bias, the majority carriers (electrons) in MoS_2 overcome the barrier to cross the junction, so the current increases with the increase of forward bias (Fig. 6(f)). That is to say, interlayer excitons current is generated through the spatially indirect separation of the interlayer excitons.

To probe visible-infrared sensitivity of the device, we have measured the magnitude of photocurrent and time resolution from the CPS/MoS_2 vdW heterostructure device illuminated under a visible-infrared laser with wavelength at 532 and 1,095 nm (Figs. 6(d)–6(g)). The observed I–V characteristics look similar to those of conventional p–n junction diode corresponding to type-II heterostructure. Meanwhile, the photodetector can be operated at low dark currents (10^{-10} A) and possesses a high photocurrent at visible range leading to high ratio of $I_{on}/I_{off} \approx 20$. In addition, the differences in the I–V results can also be viewed by plotting the current versus voltage (Ids vs. Vds) on logarithmic scale, as shown in the inset of Figs. 6(d) and 6(f). Then a rectification ratio over 10^4 under ± 2 V operating conditions is obtained. The electrical properties of low dark currents are attributed to relatively low (1.0×10^{-4} $cm^2/(V{\cdot}s)$) electron mobility of CPS measured from a field effect transistor [12] and interfacial barrier [38–39]. The important parameter to quantify the photoresponse property of the detector is the specific detectivity D^* which is defined by the equation $D^* = R\sqrt{\frac{A\Delta f}{i_n^2}}$, where A is the effective area of the detector, Δf is the electrical bandwidth, and i_n^2 is the total noise current at the same measuring condition. As the dark current is the major contributor to shot noise, D^* can be simplified to $D^* = R\sqrt{\frac{A}{2eI_{dark}}}$. Based on the measured parameters, the D^* values of the detector are approximately 3.21×10^9 Jones under 532 nm illumination and 1.35×10^9 Jones under 1,095 nm illumination at room temperature.

Light detection capability can be revealed by a spectral response at a constant intensity (20.9 mW/cm^2), as revealed in Fig. 6(h). Apparently, the heterojunction photodetector exhibits broadband photoresponse from 532 to 1,450 nm wavelength with main response locating at visible spectrum range but an response at infrared range still can be clearly observed as shown in the inset of Fig. 6(h). Heterostructure has a larger responsivity (182.7 mA/W) and fast response rates (0.05 s) to 532 nm light which can be attributed to the larger light absorption coefficient of the two materials under this wavelength. The response speed of the photodetector under different light illumination, longer than 950 nm, is almost the same in agreement with the relevant Ref. [34], as shown in Fig. 6(i). Meanwhile, this photodetector exhibits a high photocurrent about 40 pA at 1,450 nm (Fig. S6 in the ESM). It is necessary to emphasize that the detectable response beyond 950 nm wavelength can be exclusively ascribed to generate interlayer excitation because of the individual device made of pure MoS_2 or CPS device, no photoresponse is observed far beyond the corresponding bandgaps [29–30]. Meanwhile, we rule out that the observed photocurrent does not originate from the photothermal effect. One reason is that the photoresponse cutoff wavelength (1,450 nm) is consistent with interlayer bandgap (0.84 eV). If photocurrent comes from photothermal effect, we can also observe photoresponse beyond 1,450 nm wavelength. The other cause is that individual device made of pure MoS_2 or CPS device can also have photoresponse beyond its corresponding bandgaps, but we can not observe photoresponse beyond intrinsic bandgap, as shown in Fig. S7 in the ESM. Such a clearly extended response

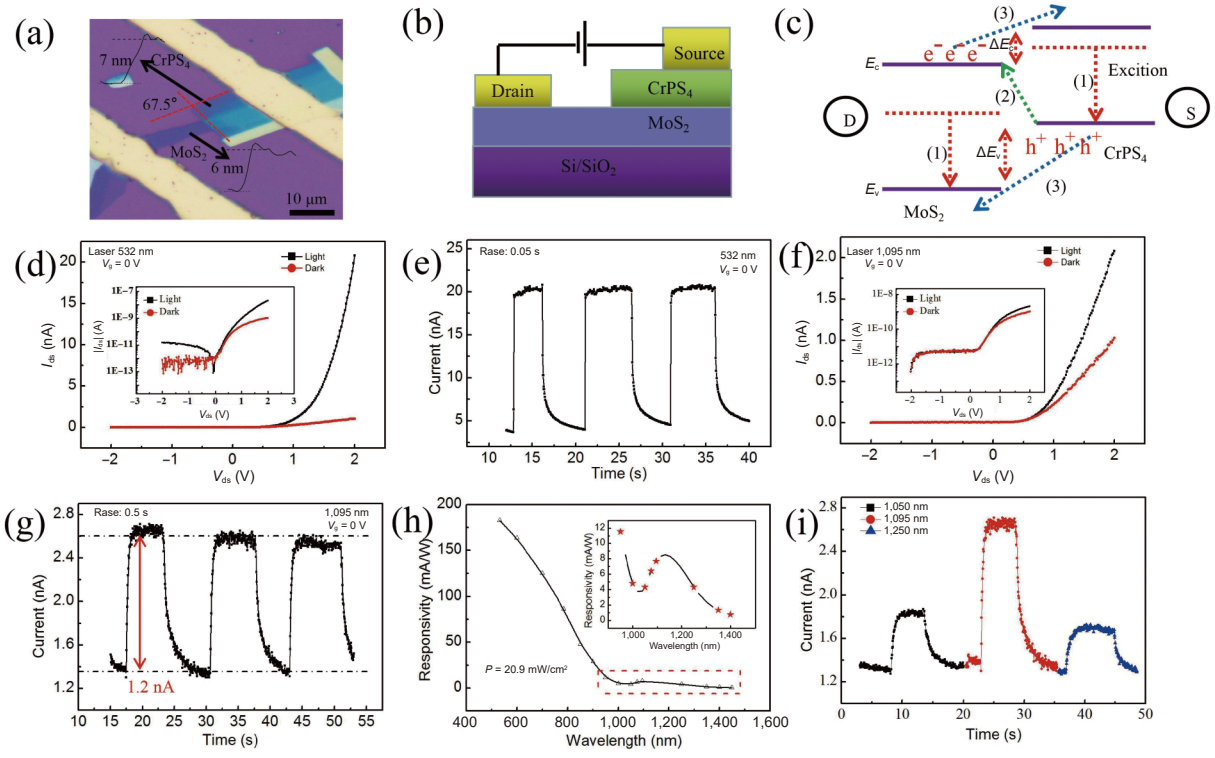

Figure 6 Photodetection performance of heterostructure. (a) The optical microscopy image of fabricated device. (b) The schematic diagram of the device structure. (c) Excitonic band alignment of the CPS/MoS_2 heterostructure under photoexcitation. (d) *I*–*V* curves of photodetector in dark and under 532 nm light illumination. The inset shows the log plots of these *I*–*V* characteristics. (e) Time-resolved photocurrent under 532 nm light. (f) *I*–*V* curves of photodetector in dark and under 1,095 nm light illumination. The inset shows the log plots of these *I*–*V* characteristics. (g) Time-resolved photocurrent under 1,095 nm light illumination. (h) Responsivity of the photodetector for wavelengths ranging from 532 to 1,450 nm. The inset shows wavelength-dependent responsivity ranging from 950 to 1,450 nm. (i) Time-resolved photocurrent under 1,050, 1,095, and 1,250 nm wavelength.

range firmly verifies interlayer transition which allows infrared excitation and infrared detection as determined by the band offset in the type-II heterostructure, instead of the intrinsic band gap limit of individual materials. In addition, one way to resonantly probe interlayer excitons and thereby determine its oscillator strength is the observation of a phenomena as interlayer exciton valley current [31–32] at interlayer coupling range as shown in the inset of Fig. 6(h) around 1,095 nm wavelength and Fig. 6(i). The valley current is caused by finite-velocity light cones on the parabolic energy dispersion. Such valley current is also observed in other heterojunction photodetectors made of $MoTe_2$-MoS_2 and WSe_2-MoS_2. Due to the small interlayer separation, the spatially separated electron and hole still experience strong Coulomb interaction resulting electrons and holes are confined to opposite layers and thus form a tightly bound interlayer exciton. Thus, the inherits valley-dependent properties of CPS/MoS_2 heterostructure present a high responsivity with 7.69 mA/W at 1,095 nm wavelength though having weak oscillator strength and momentum-indirect nature.

Interlayer coupling facilitates charge transfer between CPS and MoS_2 layers, which can readily enable us to design an infrared photodetector device because electron could transit from the VB of CPS to the CB of MoS_2 benefitting from shrinking the energy interval at the heterojunction area [35–37]. Thus, the photocurrent about 1.2 nA of device under 1,095 nm can be realized. Importantly, compared the result of this work to other interlayer coupling Type-II heterostructure recently reported from the literature, the photocurrents are orders of magnitude larger (shown in Table 1). Lastly, the anisotropic crystal structure [19] of CPS makes it sensitive to polarized light in a complex environment. Hence, by changing the relative twist angle of stacking heterostructure, the interlayer coupling response performance could further be modulated.

3 Conclusions

In the current study, we first investigated structural and electron density distribution of few-layer $CrPS_4$ single crystal synthesized by the CVT method. We then managed to fabricate the $CrPS_4$/MoS_2 heterostructure, which is a new type of interlayer coupling heterostructures. The successful fabrication of interlayer coupling heterostructure gave rise to the interlayer electron distribution. Specifically, the interlayer interactions between $CrPS_4$ and MoS_2 led to the formation of type-II heterostructure and

Table 1 The performance summary of 2D interlayer coupling-based Type-II heterostructure for infrared photodetectors

Material	Bias voltage (V)	Power density (mW/cm²)	Wavelength (nm)	Photo current (pA)	Responsivity (mA/W)	Ref.
$MoTe_2$/MoS_2	1	Not provide	1,550	15	Not provide	Zhang et al. [8]
WS_2/MoS_2	−1	2	1,030	3	8	Wang et al. [9]
WSe_2/ReS_2	−0.5	Not provide	1,250	20	Not provide	Varghese et al. [17]
GaTe/InSe	1	0.006	1,550	10	1500	Tailei Qi et al. [34]
$CrPS_4$/MoS_2	2	20.9	1,095	1,200	7.69	This work
	2	20.9	1,450	40	0.26	

interlayer charge separation, which were confirmed by the PL and KPFM experimental results. Moreover, the $CrPS_4/MoS_2$ heterostructure showed visible-infrared photoresponse between the two stacked layers. Neither $CrPS_4$ nor MoS_2 was sensitive to infrared light but their interlayer coupling shrunk the energy interval at the junction area, making the response wavelength longer than the wavelength of intrinsic components. As a result, the photocurrent effectively suppressed dark currents, as it exceeded 1,200 pA at 1,095 nm, which was several orders of magnitude higher than the photocurrents reported in multiple past studies. Our study explored both binary and ternary 2D materials devices and the fabrication process of the $CrPS_4/MoS_2$ heterostructure may increase our understanding of the interlayer coupling of 2D materials and suggest alternative approaches of creating high-performance visible-infrared optoelectronic devices.

4 Experimental

Sample preparation. Single-crystalline $CrPS_4$ was synthesized using the CVT method. Chromium (0.2461 g, 99.99%), red phosphorus (0.1466 g, 99.99%), and sulphur (0.6073, 99.99%) with a molar ratio of 1:1:4 were mixed in a vacuum-sealed quartz ampule. Next, the sealed ampoule (150 mm in length and 10 mm in diameter) was put into a two-zone furnace and was heated 24 h to 750 °C/690 °C at the same time. The source side was in the high-temperature zone, while the deposition in low-temperature zone. The ampule was kept at 750 °C/690 °C for two weeks and after that, the ampule was slowly cooled to room temperature and broken to collect the synthesized crystals, similar to the report by Jinhwan Lee et al.

Material and device characterization. The single crystal structure of CPS was characterized using XRD (Bruker D8 Advance) measurement. The TEM analysis was carried out using an HR-TEM (Titan G2 60-300 Cs-corrected TEM with EDS mapping). The heterostructures were characterized by an optical microscope (BX51, Olympus). Raman and PL measurements were performed using a WITec alpha300 RA confocal Raman microscopy system at room temperature. The power was 500 μW with a 532 nm excitation laser. The AFM and KPFM measurements were performed using Bruker MultiMode 8 Scanning Probe Microscopy with Nanoscope IV controller. A 532 nm laser was used during the KPFM analysis.

EDD calculations. The VESTA and RainbowMEM-v1.7.2 program packages were applied in the EDD calculation based on single diffraction data (X-ray double microfocal spot single crystal diffractometer, Supernova) of CPS. Then diffraction data were analyzed by using the TOPAS Academic Rietveld refinement method to '*hkl*' data file. After that, EDD was constructed by analysing '*hkl*' data file using MEM integrated in the Rainbow-MEM program.

Device fabrication and measurements. The devices were fabricated by ultraviolet (UV) lithography technology (SUSS MJB4) and Ti/Au (10 nm/50 nm) was deposited by e-beam evaporation (HHV FL400) as contact electrodes. Finally, the devices were annealed at 300 °C for 30 min under high-purity H_2 and Ar atmosphere to improve the contact quality. The electronic and photoelectronic properties were detected using a semiconductor device analyzer (Keysight B1500A). For optoelectronic measurements, the devices were illuminated with supercontinuum light source (SuperK EXTREME, NKT Photonics). The diameter of light spot was 35 μm for all wavelengths. All the tests were performed in air and at room temperature.

Acknowledgement

The authors would like to appreciate the very extensive grammar and content editing by and helpful discussions with Ziwei Zhang. This work was financially supported by the National Natural Science Foundation of China (No. NSFC 51972006).

Electronic Supplementary Material: Supplementary material (schematic illustration of growth method, EDS results at low voltage, Raman spectroscopy for $CrPS_4$, KPFM potential images in junction, photoresponse at 1,450 nm and long-period pattern in an MoS_4/CPS heterobilayer) is available in the online version of this article at https://doi.org/10.1007/s12274-021-3790-4.

References

[1] Novoselov, K. S.; Geim, A. K.; Morozov, S. V.; Jiang, D.; Zhang, Y.; Dubonos, S. V.; Grigorieva, I. V.; Firsov, A. A. Electric field effect in atomically thin carbon films. *Science* **2004**, *306*, 666–669.

[2] Dean, C. R.; Wang, L.; Maher, P.; Forsythe, C.; Ghahari, F.; Gao, Y.; Katoch, J.; Ishigami, M.; Moon, P.; Koshino, M. et al. Hofstadter's butterfly and the fractal quantum Hall effect in moiré superlattices. *Nature* **2013**, *497*, 598–602.

[3] Ma, Y. Q.; Liu, B. L.; Zhang, A. Y.; Chen, L.; Fathi, M.; Shen, C. F.; Abbas, A. N.; Ge, M. Y.; Mecklenburg, M.; Zhou, C. W. Reversible semiconducting-to-metallic phase transition in chemical vapor deposition grown monolayer WSe_2 and applications for devices. *ACS Nano* **2015**, *9*, 7383–7391.

[4] Kroemer, H. Heterostructure bipolar transistors and integrated circuits. *Proc. IEEE* **1982**, *70*, 13–25.

[5] Yu, W. J.; Liu, Y.; Zhou, H. L.; Yin, A. X.; Li, Z.; Huang, Y.; Duan, X. F. Highly efficient gate-tunable photocurrent generation in vertical heterostructures of layered materials. *Nat. Nanotechnol.* **2013**, *8*, 952–958.

[6] Zhang, C. D.; Chuu, C.; Ren, X. B.; Li, M. Y.; Li, L. J.; Jin, C. H.; Chou, M. Y.; Shih, C. Interlayer couplings, Moiré patterns, and 2D electronic superlattices in MoS_2/WSe_2 hetero-bilayers. *Sci. Adv.* **2017**, *3*, e1601459.

[7] Yu, Y. F.; Hu, S.; Su, L. Q.; Huang, L. J.; Liu, Y.; Jin, Z. H.; Purezky, A. A.; Geohegan, D. B.; Kim, K. W.; Zhang, Y. et al. Equally efficient interlayer exciton relaxation and improved absorption in epitaxial and nonepitaxial MoS_2/WS_2 heterostructures. *Nano Lett.* **2015**, *15*, 486–491.

[8] Zhang, K. N.; Zhang, T. N.; Cheng, G. H.; Li, T. X.; Wang, S. X.; Wei, W.; Zhou, X. H.; Yu, W. W.; Sun, Y.; Wang, P. et al. Interlayer transition and infrared photodetection in atomically thin Type-II $MoTe_2/MoS_2$ van der Waals heterostructures. *ACS Nano* **2016**, *10*, 3852–3858.

[9] Wang, G. C.; Li, L.; Fan, W. H.; Wang, R. Y.; Zhou, S. S.; Lü, J. T.; Gan, L.; Zhai, T. Y. Interlayer coupling induced infrared response in WS_2/MoS_2 heterostructures enhanced by surface Plasmon resonance. *Adv. Funct. Mater.* **2018**, *28*, 1800339.

[10] Ferloni, P.; Scagliotti, M. Magnetic phase transitions in iron and nickel phosphorus trichalcogenides. *Thermochim. Acta* **1989**, *139*, 197–203.

[11] Du, K. Z.; Wang, X. Z.; Liu, Y.; Hu, P.; Utama, M. I. B.; Gan, C. K.; Xiong, Q. H.; Kloc, C. Weak van der Waals stacking, wide-range band gap, and Raman study on ultrathin layers of metal phosphorus trichalcogenides. *ACS Nano* **2016**, *10*, 1738–1743.

[12] Lee, J.; Ko, T. Y.; Kim, J. H.; Bark, H.; Kang, B.; Jung, S. G.; Park, T.; Lee, Z.; Ryu, S.; Lee, C. Structural and optical properties of single- and few-layer magnetic semiconductor $CrPS_4$. *ACS Nano* **2017**, *11*, 10935–10944.

[13] Peng, Y. X.; Ding, S. L.; Cheng, M.; Hu, Q. F.; Yang, J.; Wang, F. G.; Xue, M. Z.; Liu, Z.; Lin, Z. C.; Avdeev, M. et al. Magnetic structure and metamagnetic transitions in the van der Waals antiferromagnet $CrPS_4$. *Adv. Mater.* **2020**, *32*, 2001200.

[14] Swaminathan, K.; Grassman, T. J.; Yang, L. M.; Gu, Q.; Mills, M. J.; Ringel, S. A. Optically-aligned visible/near-infrared dual-band photodetector materials and devices on GaAs using metamorphic epitaxy. *J. Appl. Phys.* **2011**, *110*, 063109.

[15] Gao, Y.; Lei, S. J.; Kang, T. T.; Fei, L. F.; Mak, C. L.; Yuan, J.; Zhang, M. G.; Li, S. J.; Bao, Q. L.; Zeng, Z. M. et al. Bias-

switchable negative and positive photoconductivity in 2D $FePS_3$ ultraviolet photodetectors. *Nanotechnology* **2018**, *29*, 244001.

[16] Hatch, S. M.; Briscoe, J.; Dunn, S. A self-powered ZnO-nanorod/CuSCN UV photodetector exhibiting rapid response. *Adv. Mater.* **2013**, *25*, 867–871.

[17] Varghese, A.; Saha, D.; Thakar, K.; Jindal, V.; Ghosh, S.; Medhekar, N. V.; Ghosh, S.; Lodha, S. Near-direct bandgap WSe_2/ReS_2 Type-II p-n heterojunction for enhanced ultrafast photodetection and high-performance photovoltaics. *Nano Lett.* **2020**, *20*, 1707–1717.

[18] Diehl, R.; Carpentier, C. D. The crystal structure of chromium thiophosphate, $CrPS_4$. *Acta Crystallogr. B* **1977**, *33*, 1399–1404.

[19] Wu, H. B.; Chen, H. P. Probing the properties of lattice vibrations and surface electronic states in magnetic semiconductor $CrPS_4$. *RSC Adv.* **2019**, *9*, 30655–30658.

[20] Budniak, A. K.; Killilea, N. A.; Zelewski, S. J.; Sytnyk, M.; Kauffmann, Y.; Amouyal, Y.; Kudrawiec, R.; Heiss, W.; Lifshitz, E. Exfoliated $CrPS_4$ with promising photoconductivity. *Small* **2020**, *16*, 1905924.

[21] Tian, N.; Yang, Y. H.; Liu, D. M.; Liu, X. L.; Tan, P. H.; Zhang, D.; Chang, K.; Li, H.; Zhao, M. J.; Li, J. R. et al. High anisotropy in tubular layered exfoliated KP_{15}. *ACS Nano* **2018**, *12*, 1712–1719.

[22] Li, S. Y.; Chen, X. Q.; Liu, F. M.; Chen, Y. F.; Liu, B. Y.; Deng, W. J.; An, B. X.; Chu, F. H.; Zhang, G. Q.; Li, S. L. et al. Enhanced performance of a CVD MoS_2 photodetector by chemical *in situ* n-type doping. *ACS Appl. Mater. Interfaces* **2019**, *11*, 11636–11644.

[23] Zhang, X.; Qiao, X. F.; Shi, W.; Wu, J. B.; Jiang, D. S.; Tan, P. H. Phonon and Raman scattering of two-dimensional transition metal dichalcogenides from monolayer, multilayer to bulk material. *Chem. Soc. Rev.* **2015**, *44*, 2757–2785.

[24] Gaur, A. P. S.; Sahoo, S.; Scott, J. F.; Katiyar, R. S. Electron–phonon interaction and double-resonance Raman studies in monolayer WS_2. *J. Phys. Chem. C* **2015**, *119*, 5146–5151.

[25] Hong, X. P.; Kim, J.; Shi, S. F.; Zhang, Y.; Jin, C. H.; Sun, Y. H.; Tongay, S.; Wu, J. Q.; Zhang, Y. F.; Wang, F. Ultrafast charge transfer in atomically thin MoS_2/WS_2 heterostructures. *Nat. Nanotechnol.* **2014**, *9*, 682–686.

[26] Wood, D. L.; Ferguson, J.; Knox, K.; Dillon, J. F. Jr. Crystal-field spectra of $d^{3,7}$ ions. III. Spectrum of Cr^{3+} in various octahedral crystal fields. *J. Chem. Phys.* **1963**, *39*, 890–898.

[27] Maturová, K.; Kemerink, M.; Wienk, M. M.; Charrier, D. S. H.; Janssen, R. A. J. Scanning kelvin probe microscopy on bulk heterojunction polymer blends. *Adv. Funct. Mater.* **2009**, *19*, 1379–1386.

[28] Gupta, S.; Batra, Y.; Mehta, B. R.; Satsangi, V. R. Study of charge separation and interface formation in a single nanorod CdS–Cu_xS heterojunction solar cell using kelvin probe force microscopy. *Nanotechnology* **2013**, *24*, 255703.

[29] Kang, J.; Tongay, S.; Zhou, J.; Li, J. B.; Wu, J. Q. Band offsets and heterostructures of two-dimensional semiconductors. *Appl. Phys. Lett.* **2013**, *102*, 012111.

[30] Gong, Y. J.; Lin, J. H.; Wang, X. L.; Shi, G.; Lei, S. D.; Lin, Z.; Zou, X. L.; Ye, G. L.; Vajtai, R.; Yakobson, B. I. et al. Vertical and in-plane heterostructures from WS_2/MoS_2 monolayers. *Nat. Mater.* **2014**, *13*, 1135–1142.

[31] Ross, J. S.; Rivera, P.; Schaibley, J.; Lee-Wong, E.; Yu, H. Y.; Taniguchi, T.; Watanabe, K.; Yan, J. Q.; Mandrus, D.; Cobden, D. et al. Interlayer exciton optoelectronics in a 2D heterostructure p–n junction. *Nano Lett.* **2017**, *17*, 638–643.

[32] Yu, H. Y.; Wang, Y.; Tong, Q. J.; Xu, X. D.; Yao, W. Anomalous light cones and valley optical selection rules of interlayer excitons in twisted heterobilayers. *Phys. Rev. Lett.* **2015**, *115*, 187002.

[33] Nayak, P. K.; Horbatenko, Y.; Ahn, S.; Kim, G.; Lee, J. U.; Ma, K. Y.; Jang, A. R.; Lim, H.; Kim, D.; Ryu, S. et al. Probing evolution of twist-angle-dependent interlayer excitons in $MoSe_2/WSe_2$ van der Waals heterostructures. *ACS Nano* **2017**, *11*, 4041–4050.

[34] Qi, T. L.; Gong, Y. P.; Li, A. L.; Ma, X. M.; Wang, P. P.; Huang, R.; Liu, C.; Sakidja, R.; Wu, J. Z.; Chen, R. et al. Interlayer transition in a vdW heterostructure toward ultrahigh detectivity shortwave infrared photodetectors. *Adv. Funct. Mater.* **2020**, *30*, 1905687.

[35] Wang, F. K.; Gao, T.; Zhang, Q.; Hu, Z. Y.; Jin, B.; Li, L.; Zhou, X.; Li, H. Q.; Van Tendeloo, G.; Zhai, T. Y. Liquid-alloy-assisted growth of 2D ternary $Ga_2In_4S_9$ toward high-performance UV photodetection. *Adv. Mater.* **2019**, *31*, 1806306.

[36] Jin, B.; Zuo, N.; Hu, Z. Y.; Cui, W. J.; Wang, R. Y.; Van Tendeloo, G.; Zhou, X.; Zhai, T. Y. Excellent excitonic photovoltaic effect in 2D $CsPbBr_3$/CdS heterostructures. *Adv. Funct. Mater.* **2020**, *30*, 2006166.

[37] Wang, F. K.; Luo, P.; Zhang, Y.; Huang, Y.; Zhang, Q. F.; Li, Y.; Zhai, T. Y. Band structure engineered tunneling heterostructures for high-performance visible and near-infrared photodetection. *Sci. China Mater.* **2020**, *63*, 1537–1547.

[38] Wang, H. L.; Wang, X. D.; Chen, Y.; Zhang, S. K.; Jiang, W.; Zhang, X.; Qin, J. J.; Wang, J.; Li, X. G.; Pan, Y. Y. et al. Extremely low dark current MoS_2 photodetector via 2D halide perovskite as the electron reservoir. *Adv. Opt. Mater.* **2020**, *8*, 1901402.

[39] Zhou, N.; Wang, R. Y.; Zhou, X.; Song, H. Y.; Xiong, X.; Ding, Y.; Lü, J. T.; Gan, L.; Zhai, T. Y. P-GaSe/N-MoS_2 vertical heterostructures synthesized by van der Waals epitaxy for photoresponse modulation. *Small* **2018**, *14*, 1702731.